

Deterministic Quantum Communication Between Fixed-Frequency Superconducting Qubits via Broadband Resonators

Takeaki Miyamura,^{1,*} Zhiling Wang,² Kohei Matsuura,¹ Yoshiki Sunada,³ Keika Sunada,¹ Kenshi Yuki,¹ Jesper Ilves,¹ and Yasunobu Nakamura^{1,2}

¹*Department of Applied Physics, Graduate School of Engineering,
The University of Tokyo, Bunkyo-ku, Tokyo 113-8656, Japan*

²*RIKEN Center for Quantum Computing (RQC), Wako, Saitama 351-0198, Japan*

³*Department of Applied Physics, Stanford University, Stanford, California 94305, USA*

(Dated: December 10, 2025)

Quantum communication between remote chips is essential for realizing large-scale superconducting quantum computers. For such communication, itinerant microwave photons propagating through transmission lines offer a promising approach. However, demonstrations to date have relied on frequency-tunable circuit elements to compensate for fabrication-related parameter variations between sender and receiver devices, introducing control complexity and limiting scalability. In this work, we demonstrate deterministic quantum state transfer and remote entanglement generation between fixed-frequency superconducting qubits on separate chips. To compensate for the sender-receiver mismatch, we employ a frequency-tunable photon-generation technique which enables us to adjust the photon frequency without modifying circuit parameters. To enhance the frequency tunability, we implement broadband transfer resonators composed of two coupled coplanar-waveguide resonators, achieving a bandwidth of more than 100 MHz. This broadband design enables successful quantum communication across a 30-MHz range of photon frequencies between the remote qubits. Quantum process tomography reveals state transfer fidelities of around 78% and Bell-state fidelities of around 73% across the full frequency range. Our approach avoids the complexity of the control lines and noise channels, providing a flexible pathway toward scalable quantum networks.

I. INTRODUCTION

Superconducting quantum computers are one of the most promising platforms for practical quantum computation [1, 2]. To realize a large-scale superconducting quantum computer, quantum communication between spatially separated quantum processors is essential [3–5]. As individual quantum processors approach fundamental limits in cooling capacity [6], control line density [7], and frequency allocation of qubits [8], modular approaches that connect multiple quantum processing units become increasingly important [9, 10]. This necessity has driven the development of quantum communication protocols for transferring quantum information and generating entanglement between remote superconducting circuits [11].

For superconducting quantum computing, two microwave-based approaches have been explored for realizing modular architecture at cryogenic temperatures. One of them exploits discrete resonance modes of a transmission line to mediate interactions between qubits [12–22]. This standing-wave approach has enabled modular quantum computing architectures, but is constrained by the physical length of the connecting cable. The other employs propagating microwave photons [23]. In this approach, quantum information is transferred by converting the sender-qubit excited state into an

itinerant microwave photon. This photon then travels along the transmission line to the receiver, where it is absorbed to complete the quantum state transfer. While this approach enables long-distance communication, it has required precise frequency alignment between the interface modes of the sender and the receiver to achieve efficient state transfer.

Various methods for quantum communication using itinerant microwave photons have been demonstrated. Microwave-driven photon-emission schemes with tunable transmons have enabled remote quantum operations [24–26] and have been demonstrated between qubits in separate dilution refrigerators [27–30]. Similarly, transmons equipped with tunable couplers for photon emission have demonstrated quantum communication capabilities [31, 32], including bidirectional multiphoton transfer [33] and chiral photon emission and absorption [34]. However, all previous implementations have relied on frequency-tunable circuit elements, such as flux-tunable transmons, to compensate for fabrication-related parameter variations and ensure resonance matching between sender and receiver. This requirement for tunability introduces additional control complexity through magnetic flux lines, creates potential decoherence channels from flux noise, and poses scaling challenges for large quantum networks [35].

In this work, we demonstrate deterministic quantum communication between fixed-frequency superconducting qubits using an itinerant microwave photon. We employ a frequency-tunable photon-generation technique [36] that adjusts the emitted-photon frequency

* miyamura@qipe.t.u-tokyo.ac.jp

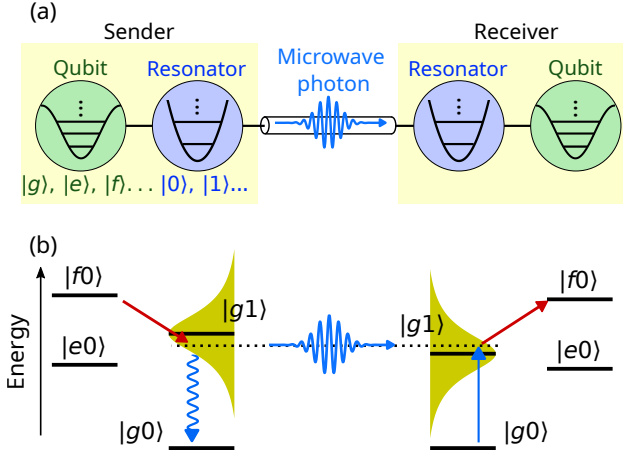


FIG. 1. Quantum communication between fixed-frequency superconducting qubits with broadband resonators. (a) Schematic of the system. (b) Energy-level diagram of the system. A microwave photon is emitted from the sender device (left) via a resonator-assisted Raman transition (red arrow) and absorbed by the receiver device (right). The broadband designs of the communication resonators (yellow Lorentzians) compensate for frequency mismatch, and the frequency-tunable photon generation method [36] enables quantum communication between fixed-frequency qubits despite such variations.

without modifying circuit parameters, thereby compensating for the fabrication-related frequency mismatch between the sender and the receiver. To extend the operational bandwidth of this frequency-tuning approach, we design broadband transfer resonators composed of two coupled coplanar-waveguide resonators, achieving a bandwidth exceeding 100 MHz. This design allows us to compensate for the fabrication-related frequency offset of 50 MHz between the sender and the receiver and demonstrate successful quantum communication. Across the 30-MHz frequency span where the sender and receiver bandwidths overlap, we demonstrate quantum state transfer with process fidelities of approximately 78% and remote entanglement generation with Bell-state fidelities of approximately 73%. Our approach eliminates the need for flux-tunable circuit elements and their associated control complexity and noise channels, providing a scalable pathway toward quantum networks based on fixed-frequency qubits.

II. QUANTUM COMMUNICATION BETWEEN FIXED-FREQUENCY QUBITS

A. Basic concept

Figure 1 shows the quantum communication scheme employed in this work. Two fixed-frequency transmon qubits [37] are connected via transfer resonators and a transmission line. Here, $|g\rangle$, $|e\rangle$, and $|f\rangle$ denote the three

lowest eigenstates of the qubit, while $|0\rangle$ and $|1\rangle$ represent the resonator Fock states. The communication protocol utilizes a resonator-assisted Raman transition [38, 39], enabling the sender device to emit a photon carrying quantum information and the receiver device to absorb it. Efficient transfer requires precise frequency matching between the transfer resonators, which is challenging due to fabrication-related parameter variations [40, 41]. We address this frequency-matching requirement by employing a frequency-tunable photon-generation method for fixed-frequency devices [36]. By off-resonantly driving the $|f0\rangle$ - $|g1\rangle$ transition, the emitted-photon frequency can be adjusted to match the transfer-resonator frequency, thereby enabling communication. As long as the frequencies of the transfer resonators lie within their bandwidths, the sender and the receiver can communicate at a matching frequency.

B. Design of the transfer resonator

The device used in this work is shown in Fig. 2(a) and is composed of a fixed-frequency transmon qubit coupled to a readout resonator and a transfer resonator for single-photon emission and absorption.

To enable quantum communication across a wide frequency range, we implement transfer resonators with enhanced bandwidth. Each transfer resonator consists of two coupled coplanar resonators designed to provide a large combined bandwidth. In the following, we denote the frequency (linewidth) of the first resonance mode of the coupled resonators as ω_+ (κ_+) and that of the second resonance mode as ω_- (κ_-) [Fig. 2(d)]. These modes are the eigenmodes obtained through diagonalization of the two coupled resonator modes, excluding the external coupling of the outer resonator.

The two-resonator configuration allows various strategies depending on the design priorities. In this work, we demonstrate two different approaches for the sender and receiver devices. For the receiver device, we choose to prioritize a broad operational bandwidth with a flat spectral response. To achieve this, we aim to position the two resonator modes with a frequency separation equal to their individual linewidths, i.e., $\omega_+ = \omega_- + \kappa_-$ and $\kappa_+/2\pi = \kappa_-/2\pi = 100$ MHz. This configuration creates response of a second-order Butterworth filter that maintains a flat resonator spectrum over an extended frequency range [42] [Fig. 2(e)].

For the sender device, we choose to maximize the frequency-tunable range while maintaining sufficient photon-emission rate. Following the formalism developed in Ref. 36, the photon-emission rate is defined as the decay rate of the $|f\rangle$ state under the $|f0\rangle$ - $|g1\rangle$ drive in the adiabatic limit. When two resonators are contributing to photon emission, the analytical form of this rate Γ_f is calculated as

$$\Gamma_f = \frac{4g_{\text{eff}}^2(X^2\kappa_+\delta_+ + Y^2\kappa_-\delta_-)}{4\delta_+^2\delta_-^2 + (\kappa_+\delta_+ + \kappa_-\delta_-)^2}, \quad (1)$$

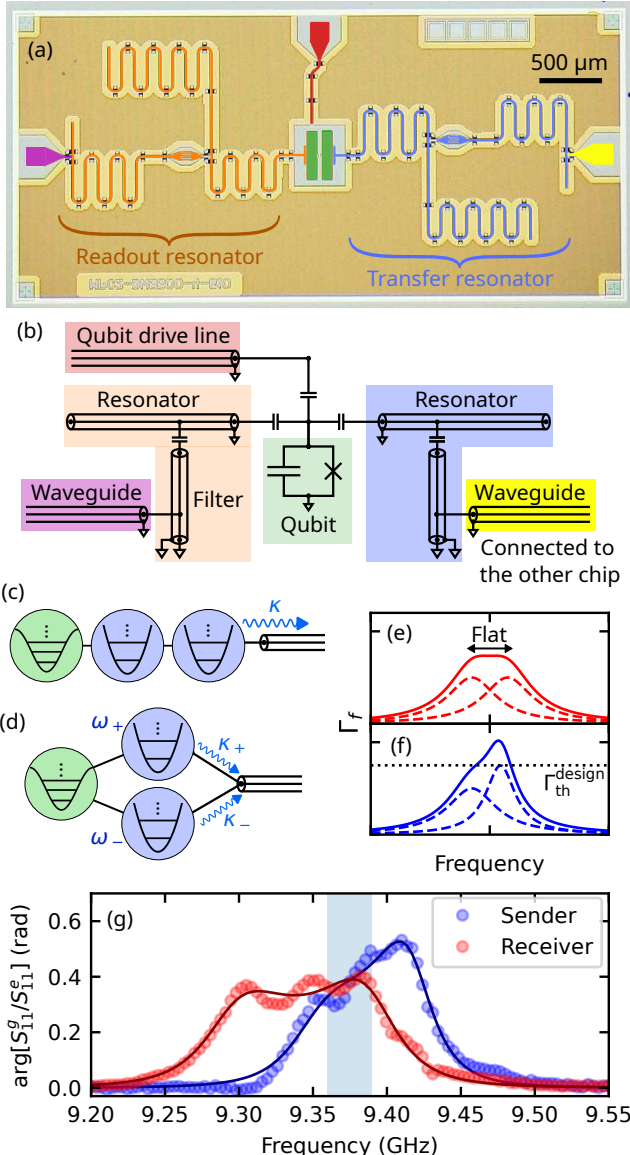


FIG. 2. (a) False-colored photograph of the device. A fixed-frequency transmon qubit (green) is capacitively coupled to a readout resonator (orange) and a transfer resonator for single-photon emission and absorption. The qubit is driven via a dedicated control line (red). Both the sender and receiver devices have the same circuit structure. (b) Equivalent circuit diagram of each device. (c) Schematic of the qubit–transistor-resonator system. (d) Equivalent schematic of (c). (e)(f) Resonator design strategies employed in this work. Γ_f is the photon emission rate that corresponds to the resonator spectrum. Dashed curves represent individual resonance modes and solid curves represent the combined resonator spectrum. The black dotted line indicates the threshold of the photon-emission rate used for designing. (g) Reflection spectroscopy of the transfer resonator. The qubit is prepared in the $|g\rangle$ ($|e\rangle$) state, and the reflection coefficient $S_{11,g(e)}$ is measured. Blue (red) dots represent the phase of the ratio $S_{11,g}/S_{11,e}$ for the sender (receiver) device, with corresponding fits shown as solid lines. The shaded region indicates the frequency range of the emitted photons used in the quantum communication experiments.

where δ_{\pm} is the detuning between ω_{\pm} and the emitted-photon frequency ω_{ph} , g_{eff} is the effective $|f0\rangle$ – $|g1\rangle$ coupling strength, and X and Y are the transformation coefficients obtained from diagonalizing the two resonator modes. The derivation of Eq. (1) and the definitions of X and Y are provided in Appendix B. We optimize the resonator parameters to maximize the frequency range over which Γ_f exceeds a specified threshold of $\Gamma_{\text{th}}^{\text{design}}/2\pi = 8$ MHz [Fig. 2(f)]. Details on the optimization can be found in Appendix B 2. We note that Eq. (1) implies a trade-off between the resonator bandwidth and the photon-emission rate. Therefore, enhancing the photon-emission rate leads to a reduction in the resonator bandwidth.

To enable quantum communication across a wide frequency range, both devices are targeted to the same resonance frequencies and are designed to maximize spectral overlap. Figure 2(g) presents the measured transfer-resonator spectra for both devices. Both resonators exhibit a bandwidth exceeding 100 MHz. The bandwidth of the sender device is made narrower in order to maintain the photon-emission rate above a threshold. The receiver device achieves a broader linewidth of approximately 150 MHz and a flatter resonator spectrum as intended by the design strategy. Despite the fabrication-related frequency offset of approximately 50 MHz between the sender and the receiver, the spectral overlap between the two devices indicates the capability of performing quantum communication.

If only one resonator were used to realize a photon-emission bandwidth of 100 MHz, the corresponding linewidth of the resonator would have enhanced the energy relaxation of the qubit through off-resonant Purcell effect. By using the two resonator configuration, we provide a band-pass filtering effect that suppresses unwanted decay at the qubit frequency [43, 44]. To further mitigate the Purcell decay, we implement intrinsic Purcell filters [45–47], which strongly suppress the coupling between the qubit and the transmission line at the qubit frequency while maintaining efficient photon emission and absorption at the transfer-resonator frequencies. As a result, the qubit energy relaxation times average around 20 μ s (Table I), which is sufficient for demonstrating quantum communication protocols.

III. EXPERIMENT

To verify the broadband operation of our system, we demonstrate quantum communication at photon frequencies of $\omega_{\text{ph}}/2\pi = 9.36, 9.37, 9.38$, and 9.39 GHz, all within the spectral overlap region of the transfer resonators shown in Fig. 2(g). The target photon waveform is set to $\psi_{\text{ph}}^{\text{target}}(t) = \sqrt{\kappa_{\text{ph}}/2} \operatorname{sech}(\kappa_{\text{ph}} t)$ with $\kappa_{\text{ph}}/2\pi = 2$ MHz.

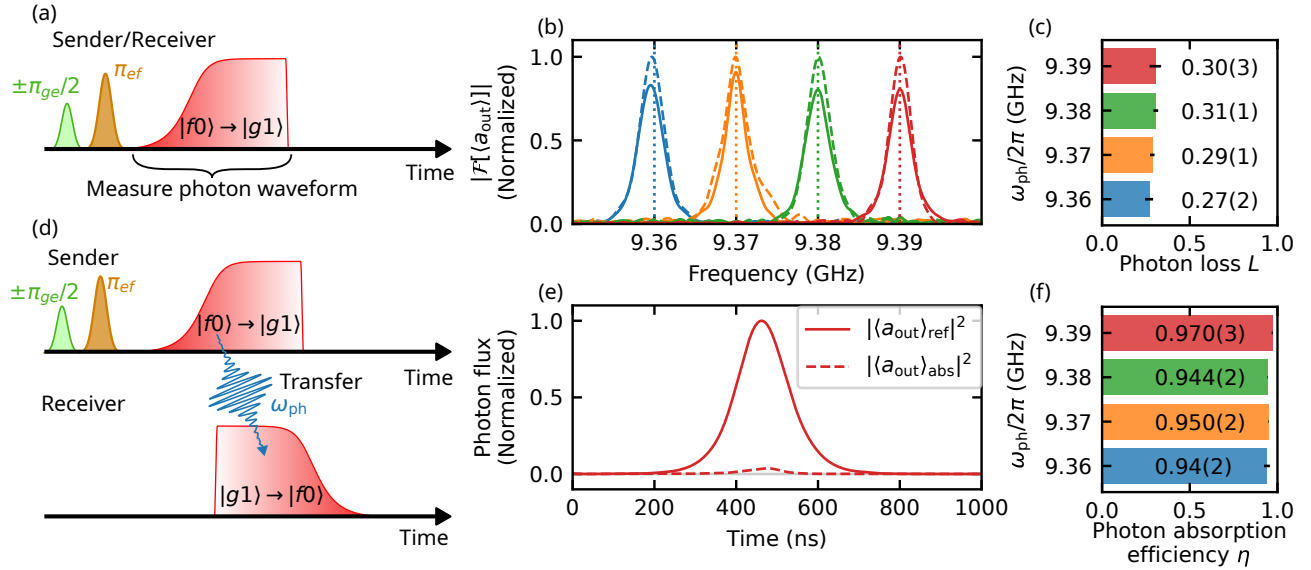


FIG. 3. Propagation loss and absorption efficiency. (a) Pulse sequence to estimate photon loss during propagation. A microwave photon is emitted from the sender and receiver devices separately. The presence of a circulator in the connecting cable (see Fig. 5 in Appendix A) allows an independent measurement of photon loss during propagation and absorption efficiency at the receiver [24]. (b) Fourier amplitudes of the emitted photons at each target frequency ω_{ph} . Solid curves represent photons emitted from the sender device, while dashed curves represent photons emitted from the receiver device. Vertical dotted lines indicate the target photon frequencies ω_{ph} . (c) Estimated photon loss for each photon frequency ω_{ph} . (d) Pulse sequence for measuring the photon-absorption efficiency. A microwave photon emitted from the sender is absorbed at the receiver using a time-reversed drive pulse. (e) Measured photon flux at $\omega_{\text{ph}}/2\pi = 9.39$ GHz. The solid curve shows the photon flux without absorption, and the dashed curve shows the residual photon flux after the absorption at the receiver. (f) Measured absorption efficiency for each photon frequency ω_{ph} .

A. Photon emission and absorption at multiple photon frequencies

First, we estimate the photon loss during propagation through the transmission line. The loss can be determined by emitting a single photon individually from either the sender or receiver device, exploiting the presence of a circulator in the connecting cable [24] (see Fig. 5 for the measurement setup). The pulse sequence for this measurement is shown in Fig. 3(a). To observe the photon waveform $\langle a_{\text{out}}(t) \rangle$, we prepare the qubit in the superposition state $(|g\rangle \pm |f\rangle)/\sqrt{2}$. The emitted microwave field is amplified using a flux-driven Josephson parametric amplifier (JPA) [48]. We perform this measurement 2×10^5 times for each state and average the results to obtain the photon waveform [36].

This approach assumes that both devices emit photons with equal efficiency. However, characterization of our devices reveals deviations from this assumption. In particular, the receiver device sometimes exhibits an unexpectedly large decay from the $|f\rangle - |e\rangle$ transition and leakage to states beyond $|f\rangle$ during photon emission (see Appendix C 2). To account for this qubit-population imbalance, we measure the qubit population after the photon emission. Assuming that the population in $|g\rangle$ (P_g) after the emission equals the average emitted photon number, we correct for the population imbalance by

normalizing the observed photon waveform by $\sqrt{P_g}$.

Figure 3(b) shows the Fourier transforms of the emitted photons. The measured frequencies of the emitted photons from both devices align well with the target photon frequencies. The photon loss is quantified using the relation

$$L = 1 - \frac{\int |\langle a_{\text{out}}(t) \rangle_{\text{tx}}|^2 dt}{\int |\langle a_{\text{out}}(t) \rangle_{\text{rx}}|^2 dt}, \quad (2)$$

where $\langle a_{\text{out}}(t) \rangle_{\text{tx(rx)}}$ is the expectation value of the field operator on the transmission line when emitting a photon from the sender (receiver). The measured photon loss at each frequency is presented in Fig. 3(c). The loss shows insignificant frequency dependence across the measured range, yielding an average value of 29%, which is used in the numerical simulations in Sec. III B.

To characterize the absorption efficiency, we perform photon emission and absorption measurements at the same set of frequencies. The pulse sequence for photon absorption is shown in Fig. 3(d). The delay between the two $|f\rangle - |g\rangle$ drives is optimized to maximize the population in the receiver's $|f\rangle$ state. Following photon emission from the sender, we either enable or disable the absorption at the receiver and monitor the reflected waveform through the circulator. When the absorption is enabled, the reflected waveform corresponds to the photon flux that is not absorbed by the receiver, whereas

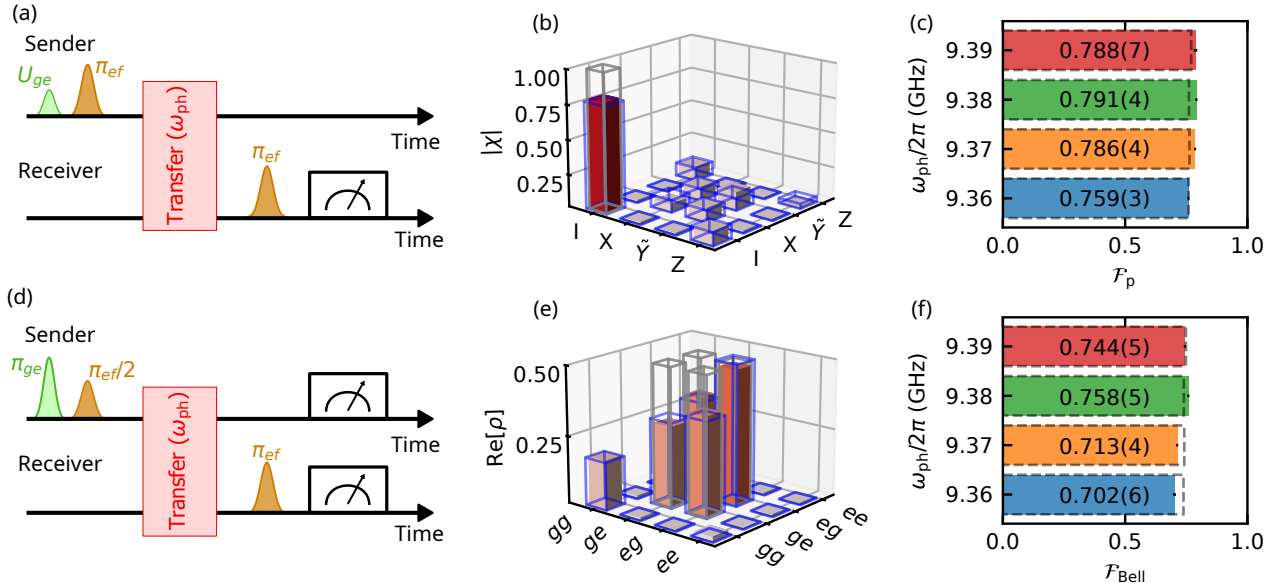


FIG. 4. Quantum state transfer and remote entanglement generation. (a) Pulse sequence for quantum state transfer between the sender and receiver qubits. (b) Process matrix for quantum state transfer at $\omega_{\text{ph}}/2\pi = 9.39$ GHz. Gray and blue wireframes indicate the ideal process and the simulated result, respectively. (c) Process fidelities for quantum state transfer at each photon frequency ω_{ph} . The dashed frames represent the simulated results. (d) Pulse sequence for remote Bell-state generation. (e) Reconstructed density matrix of the two-qubit Bell state at $\omega_{\text{ph}}/2\pi = 9.39$ GHz. Gray and blue wireframes indicate the ideal state and the simulated result, respectively. (f) Bell-state fidelities at each photon frequency ω_{ph} . The dashed frames indicate the simulated results.

without the absorption, it corresponds to the total photon flux arriving at the receiver. Figure 3(e) presents the measured photon flux at $\omega_{\text{ph}}/2\pi = 9.39$ GHz with and without the absorption. The absorption efficiency η is calculated as

$$\eta = 1 - \frac{\int |\langle a_{\text{out}}(t) \rangle_{\text{abs}}|^2 dt}{\int |\langle a_{\text{out}}(t) \rangle_{\text{ref}}|^2 dt}, \quad (3)$$

where $\langle a_{\text{out}}(t) \rangle_{\text{abs(ref)}}$ represents the expectation value of the field operator with (without) the absorption at the receiver. The absorption efficiency at each photon frequency is shown in Fig. 3(f) and is approximately 95% across the measured frequency range.

B. Deterministic quantum state transfer and generation of remote entanglement

Next we demonstrate quantum state transfer and remote entanglement generation between the fixed-frequency qubits.

The pulse sequence for quantum state transfer is shown in Fig. 4(a). We prepare six cardinal qubit states at the sender: $|\psi\rangle = |g\rangle, |e\rangle, |\pm\rangle, |\pm i\rangle$, where $|\pm\rangle = (|g\rangle \pm |e\rangle)/\sqrt{2}$ and $|\pm i\rangle = (|g\rangle \pm i|e\rangle)/\sqrt{2}$. Following the state preparation, we transfer the quantum state from the sender to the receiver via a microwave photon at frequency ω_{ph} , followed by an application of a π_{ef} pulse at the receiver to complete the protocol. Quantum process tomography [49] is performed by preparing the input

states at the sender and measuring the output states at the receiver. Figure 4(b) presents the reconstructed process matrix χ when the transfer is mediated by a photon at $\omega_{\text{ph}}/2\pi = 9.39$ GHz. The process fidelity \mathcal{F}_p for state transfer using photons at various frequencies is shown in Fig. 4(c), achieving values around 78%. The consistent fidelities across the 30-MHz frequency range demonstrate that the communication protocol performs similarly regardless of the specific photon frequency within the operational bandwidth.

To understand the sources of infidelity, we perform numerical simulations (see Appendix C4) using the measured photon loss, absorption efficiency from Sec. III A, and the device coherence times listed in Table I. The simulated results, shown as blue frames in Figs. 4(b) and (e), agree well with the experimental data. The analysis of the simulation reveals that the infidelity originates from photon loss during propagation ($\approx 15\%$), imperfect photon absorption at the receiver (1.5–3.0%), qubit energy relaxation ($\approx 1.8\%$), and qubit dephasing ($\approx 2.6\%$).

In addition to quantum state transfer, we demonstrate remote entanglement generation. The pulse sequence for creating a Bell state between the remote qubits is shown in Fig. 4(d). We perform two-qubit state tomography to characterize the generated entangled state. Figure 4(e) displays the reconstructed density matrix of the two-qubit system when the communication is mediated by a photon at $\omega_{\text{ph}}/2\pi = 9.39$ GHz. The Bell-state fidelity $\mathcal{F}_{\text{Bell}}$ for entanglement generation using photons at different frequencies is summarized in Fig. 4(f). The fidelities

ties are approximately constant across the measured frequency range, with an average of 73%. However, slightly lower fidelities are observed for communication mediated by photons at $\omega_{\text{ph}}/2\pi = 9.36$ and 9.37 GHz. We attribute this reduction to temporal fluctuations in qubit coherence during these measurements. Repeated characterization of our devices reveals occasional degradation of coherence times, with values as low as $T_{1,ge} \sim 10\ \mu\text{s}$ and $T_{1,ef} \sim 3\ \mu\text{s}$ (see Appendix A), compared to the typical values listed in Table I. The origin of these coherence time fluctuations is not definitively established. We suspect coupling to a two-level-system (TLS) defect, as we occasionally observe sudden shifts in qubit frequency with these devices, a characteristic signature of TLS effects [50–52]. Indeed, numerical simulations including the degraded coherence times yield infidelity contributions from photon loss ($\approx 15\%$), imperfect photon absorption (1.5–3.0%), qubit energy relaxation (0.7–4.8%), and qubit dephasing (4.2–10%), consistent with the observed Bell-state fidelities.

IV. DISCUSSION

We have demonstrated deterministic quantum communication between fixed-frequency superconducting transmon qubits using itinerant microwave photons. By implementing each transfer resonator as two coupled coplanar resonators that simultaneously contribute to the photon emission or absorption process, we achieved resonator bandwidths of approximately 150 MHz for the receiver and 100 MHz for the sender. Despite the fabrication-related frequency offset of 50 MHz between devices, the broadband design provided a 30-MHz spectral overlap. Across this overlapped frequency range ($\omega_{\text{ph}}/2\pi = 9.36$ –9.39 GHz), the photon absorption efficiency remained stable at approximately 95%. Both quantum state transfer and remote entanglement generation were successfully demonstrated, achieving process fidelities around 78% and Bell-state fidelities around 73%, respectively. The consistent performance across the frequency range confirms that our approach eliminates the need for flux-tunable circuit elements while maintaining a consistent communication fidelity, establishing a practical pathway toward scalable quantum communication networks based on fixed-frequency qubits. Our approach is particularly advantageous for 3D integrated architectures where magnetic flux lines require specialized implementation [53, 54].

The distinct resonator designs for the sender and the receiver devices suggest the spectral engineering flexibility enabled by the two-resonator configuration. The design approaches address the fundamental trade-off between operational bandwidth and photon-emission rate: broader bandwidth enables photon emission and absorption across an extended frequency range, while narrower bandwidths, within the limits of the adiabatic condition, make it easier to achieve higher photon-emission rates for

faster communication [Eq. (1)]. This flexibility allows optimization according to specific application requirements, such as prioritizing broad operational bandwidth or enabling faster communication protocols. Moreover, extending this approach to configurations with more than two coupled resonators could potentially offer enhanced design flexibility for spectral engineering.

The broad operational bandwidth opens new possibilities for frequency-multiplexed quantum communication, where multiple quantum channels operate simultaneously at different carrier frequencies within the same transmission line. A recent theoretical study indicates that microwave waveguides can support multiple concurrent quantum channels when photons are appropriately spaced in frequency, with simulations suggesting the potential for tens of multiplexed channels [55]. Combined with our frequency-tunable photon generation method, dense frequency-division multiplexing significantly increases communication capacity. Beyond multiplexed state transfer, the extended frequency-tunable range enabled by the broadband resonator design facilitates frequency-bin encoded quantum information processing [56] and the generation of frequency-domain cluster states [57, 58] for measurement-based quantum computation.

The frequency tunability also addresses practical challenges in device operation. When a strongly coupled TLS defect [59] is present near the transfer-resonator frequency, the $|f0\rangle-|g1\rangle$ drive can excite the TLS instead of emitting photons, significantly degrading photon emission and absorption. Our approach enables in-situ avoidance of such TLS defects by adaptively selecting photon frequencies that minimize interaction with specific defect resonances, without requiring hardware modifications or device retuning.

Finally, we note that the photon bandwidth in this work ($\kappa_{\text{ph}}/2\pi = 2\ \text{MHz}$) is narrower than those demonstrated in previous studies [24, 28, 38]. This limitation arises from the adiabatic condition underlying our wave-packet shaping method [36]. Extending non-adiabatic wave-packet shaping techniques to the off-resonant driving scheme enables faster quantum communication while maintaining the flexibility of frequency-tunable photon generation.

ACKNOWLEDGMENTS

We thank A. Kulikov, X. Dai and A. Hernandez for the advices for improving the experiments, and R. Araki, K. Uchida for the fruitful discussions. This work was supported in part by the University of Tokyo Forefront Physics and Mathematics Program to Drive Transformation (FoPM), a World-leading Innovative Graduate Study (WINGS) Program, the Ministry of Education, Culture, Sports, Science and Technology (MEXT) Quantum Leap Flagship Program (Q-LEAP) (Grant No. JPMXS0118068682), the JSPS Grant-in-Aid for Scientific

Research (KAKENHI) (Grant No. JP22H04937), and the JST CREST (Grant No. JPMJCR23I4).

Appendix A: EXPERIMENTAL SETUP

The measurement setup used in this work is shown in Fig. 5. The sender and receiver devices are connected via a flexible NbTi coaxial cable (Koaxis, CC086NBTI) with a circulator inserted between them to enable independent characterization of photon emission, propagation loss, and absorption efficiency. The flexible cable uses a niobium-titanium-alloy center conductor with a silver-plated copper-braid shield and PTFE dielectric. For transfer resonator spectroscopy, the readout line of the sender device is manually reconfigured by connecting it to a dedicated probe line.

Several components in the setup are shared between different measurement configurations to minimize hardware complexity. The local oscillator (LO) for the sender qubit readout and for observing the photon waveform is common in both measurement modes. Consequently, the LO frequency must be alternatively adjusted depending on the measurement configuration: 10.050 GHz for the sender-qubit readout and 9.480 GHz for photon-waveform observation. Similarly, the AWG, LO, and frequency doubler used for the pump of the JPA are shared between the sender readout chain and the photon observation chain. The LO frequencies for the $|f0\rangle - |g1\rangle$ drives and the qubit control drives are chosen to enable observation of the photon waveform [60].

The device parameters are listed in Table I. The energy relaxation times listed in the table represent typical values observed during the experiments. However, we occasionally observe sudden degradation in coherence times. To provide a complete characterization of the device stability, we report the full range of observed T_1 values. For the sender device, $T_{1,ge}$ ranged from 6 to 31 μ s, and $T_{1,ef}$ ranged from 2.4 to 11 μ s. For the receiver device, $T_{1,ge}$ ranged from 13 to 25 μ s, and $T_{1,ef}$ ranged from 3.5 to 13.5 μ s. These fluctuations are consistent with the reduction in communication fidelity observed at certain photon frequencies, as discussed in Sec. III B.

Appendix B: DESIGNING TRANSFER RESONATORS

1. Derivation of Γ_f in case of two resonators

We derive the photon emission rate Γ_f for a transmon qubit coupled to two coplanar resonators connected to a transmission line. The system Hamiltonian is

$$\mathcal{H} = \mathcal{H}_q + \mathcal{H}_r + \mathcal{H}_f + \mathcal{H}_b + \mathcal{H}_{qr}^c + \mathcal{H}_{rf}^c + \mathcal{H}_{fb}^c, \quad (B1)$$

TABLE I. Device parameters.

Parameter	Sender	Receiver
Qubit frequency $\omega_{eg}/2\pi$ (GHz)	7.982	8.199
Qubit anharmonicity $\alpha/2\pi$ (MHz)	356	352
Readout resonator frequency $\omega_r/2\pi$ (GHz)	10.14	10.50
Readout filter frequency $\omega_f/2\pi$ (GHz)	10.06	10.70
Resonator-resonator coupling $J/2\pi$ (MHz)	44	191
Readout filter linewidth $\kappa_f/2\pi$ (MHz)	81	290
Transfer resonator frequency $\omega_t/2\pi$ (GHz)	9.393	9.348
Transfer filter frequency $\omega_f/2\pi$ (GHz)	9.380	9.341
Transfer-resonator coupling $J/2\pi$ (MHz)	44	58
Transfer filter linewidth $\kappa_f/2\pi$ (MHz)	120	137
Qubit-readout-resonator coupling strength $g_{qr}/2\pi$ (MHz)	151	242
Qubit-transfer-resonator coupling strength $g_{qt}/2\pi$ (MHz)	159	142
$ g\rangle - e\rangle$ energy-relaxation time $T_{1,ge}$ (μ s)	20(6)	18(2)
$ g\rangle - e\rangle$ Ramsey dephasing time $T_{2,ge}^*$ (μ s)	22(2)	15(4)
$ g\rangle - e\rangle$ echo dephasing time $T_{2,ge}^e$ (μ s)	22(6)	29(5)
$ e\rangle - f\rangle$ energy-relaxation time $T_{1,ef}$ (μ s)	7.6(2.5)	8.6(2.8)
$ e\rangle - f\rangle$ Ramsey dephasing time $T_{2,ef}^*$ (μ s)	7.3(2.3)	5.9(1.5)

where each term represents

$$\mathcal{H}_q/\hbar = \omega_{eg} b^\dagger b + \frac{\alpha}{2} b^\dagger b^\dagger b b, \quad (B2a)$$

$$\mathcal{H}_r/\hbar = \omega_r a^\dagger a, \quad (B2b)$$

$$\mathcal{H}_f/\hbar = \omega_f f^\dagger f, \quad (B2c)$$

$$\mathcal{H}_b/\hbar = \int d\omega \omega b_\omega^\dagger b_\omega, \quad (B2d)$$

$$\mathcal{H}_{qr}^c/\hbar = g(b^\dagger a + ba^\dagger), \quad (B2e)$$

$$\mathcal{H}_{rf}^c/\hbar = J(a^\dagger f + af^\dagger), \quad (B2f)$$

$$\mathcal{H}_{fb}^c/\hbar = i\sqrt{\frac{\kappa}{2\pi}} \int d\omega (b_\omega f^\dagger - b_\omega^\dagger f). \quad (B2g)$$

Here, a , f , b are the annihilation operators for the first resonator, second resonator, and qubit, respectively, and b_ω represents the annihilation operator for the continuum modes of the transmission line. The parameters ω_{eg} , ω_r , ω_f are the qubit transition frequency and resonator frequencies, α is the qubit anharmonicity, g is the qubit-resonator coupling, J is the inter-resonator coupling, and κ is the external decay rate of the second resonator.

To analyze the coupled resonator system, we diagonalize $\mathcal{H}_{rf} = \mathcal{H}_r + \mathcal{H}_f + \mathcal{H}_{rf}^c$. This yields new eigenmodes with annihilation operators a_\pm and eigenfrequencies

$$\omega_\pm = \frac{\omega_r + \omega_f}{2} \pm \frac{1}{2} \sqrt{\Delta_{fr}^2 + 4J^2}, \quad (B3)$$

where $\Delta_{fr} = \omega_f - \omega_r$. The original operators are related to the eigenmodes through $a = Xa_- + Ya_+$ and $f = Za_- + Wa_+$, with transformation coefficients satisfying $X^2 + Y^2 = 1$ and $Z^2 + W^2 = 1$.

This transformation yields effective decay rates for each eigenmode:

$$\kappa_- = \kappa Z^2, \quad \kappa_+ = \kappa W^2, \quad (B4)$$

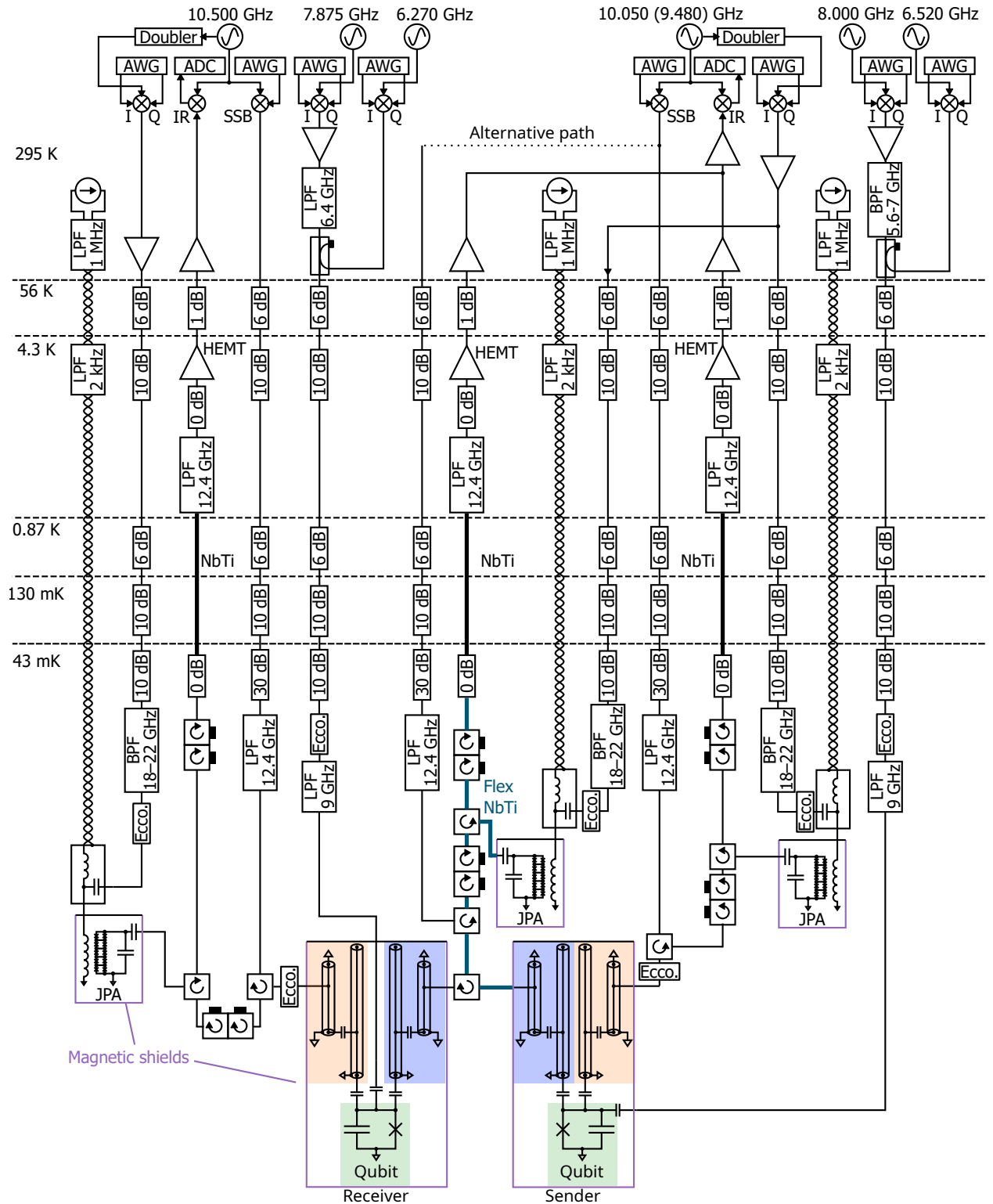


FIG. 5. Experimental setup. AWG, arbitrary waveform generator; ADC, analog-to-digital converter; SSB, single-sideband mixer; IR, image-reject mixer; LPF, low-pass filter; BPF, band-pass filter; HEMT, high-electron-mobility transistor; Ecco., eccosorb filter; JPA, Josephson parametric amplifier. The dotted line indicates the alternative signal path used for transfer resonator spectroscopy, which is manually connected by reconfiguring the sender readout line.

where κ is the external decay rate of the outer resonator.

Under microwave driving at frequency ω_d , we work in the rotating frame where the qubit Hamiltonian becomes

$$\mathcal{H}_q/\hbar = \delta_{eg} b^\dagger b + \frac{\alpha}{2} b^\dagger b^\dagger b b + \frac{\Omega}{2} (b + b^\dagger), \quad (\text{B5})$$

with $\delta_{eg} = \omega_{eg} - \omega_d$ and drive strength Ω . First-order perturbation theory yields drive-dressed eigenstates ($|\tilde{g}\rangle$, $|\tilde{e}\rangle$, and $|\tilde{f}\rangle$) and modifies the $|f\rangle - |g\rangle$ transition frequency to $\tilde{\delta}_{fg} = 2\tilde{\omega}_{eg} + \alpha - 2\omega_d$, where $\tilde{\omega}_{eg}$ is the ac-Stark-shifted qubit frequency.

The photon emission rate is obtained by solving the quantum Langevin equations for the eigenmodes a_\pm :

$$\frac{da_-}{dt} = \left(-i\Delta_- - \frac{\kappa_-}{2} \right) a_- - \frac{\sqrt{\kappa_- \kappa_+}}{2} a_+ - \sqrt{\kappa_-} b_{\text{in}}, \quad (\text{B6a})$$

$$\frac{da_+}{dt} = \left(-i\Delta_+ - \frac{\kappa_+}{2} \right) a_+ - \frac{\sqrt{\kappa_- \kappa_+}}{2} a_- - \sqrt{\kappa_+} b_{\text{in}}, \quad (\text{B6b})$$

where $\Delta_\pm = \omega_\pm - \omega_d$ and $b_{\text{in}}(t)$ is the input field from the transmission line.

Fourier transforming these equations and assuming white noise input yields the frequency-domain response functions:

$$R_\pm(\omega) = \frac{-i\sqrt{\kappa_\pm}(\omega - \Delta_\mp)}{\left[(\omega - \Delta_+) + \frac{i\kappa_-}{2} \right] \left[(\omega - \Delta_-) + \frac{i\kappa_+}{2} \right] + \frac{\kappa_+ \kappa_-}{4}}. \quad (\text{B7})$$

Applying Fermi's golden rule, the total photon emission rate is

$$\Gamma_f = g_{\text{eff}}^2 \left(X^2 |R_-(\tilde{\delta}_{fg})|^2 + Y^2 |R_+(\tilde{\delta}_{fg})|^2 \right), \quad (\text{B8})$$

where $g_{\text{eff}} = g |\langle \tilde{g} | b | \tilde{f} \rangle|$ is the effective coupling strength between the dressed states [39].

By explicitly evaluating $|R_\pm(\tilde{\delta}_{fg})|^2$ and substituting into Eq. (B8), we obtain Eq. (1) in the main text.

2. Resonator design strategy including photon-emission rate

One of the design strategies described in Sec. B 2 involves maximizing the frequency range over which the photon-emission rate Γ_f exceeds a specified threshold. To implement this approach, we use Eq. (1) to search for optimal resonator parameters.

We define the design objective as maximizing the frequency range of the emitted photon ω_{ph} where $\Gamma_f(\omega_{\text{ph}})/2\pi \geq \Gamma_{\text{th}}^{\text{design}}/2\pi = 8$ MHz. For the optimization, we fix the target resonance frequencies of both resonators to $\omega_r/2\pi = \omega_f/2\pi = 9.5$ GHz and set the qubit-resonator coupling strength to $g/2\pi = 220$ MHz, which are typical design values for our circuit architecture. The ac Stark shift is not included in this analysis. To calculate Γ_f , we set the drive strength to $\Omega/2\pi = 1$ GHz,

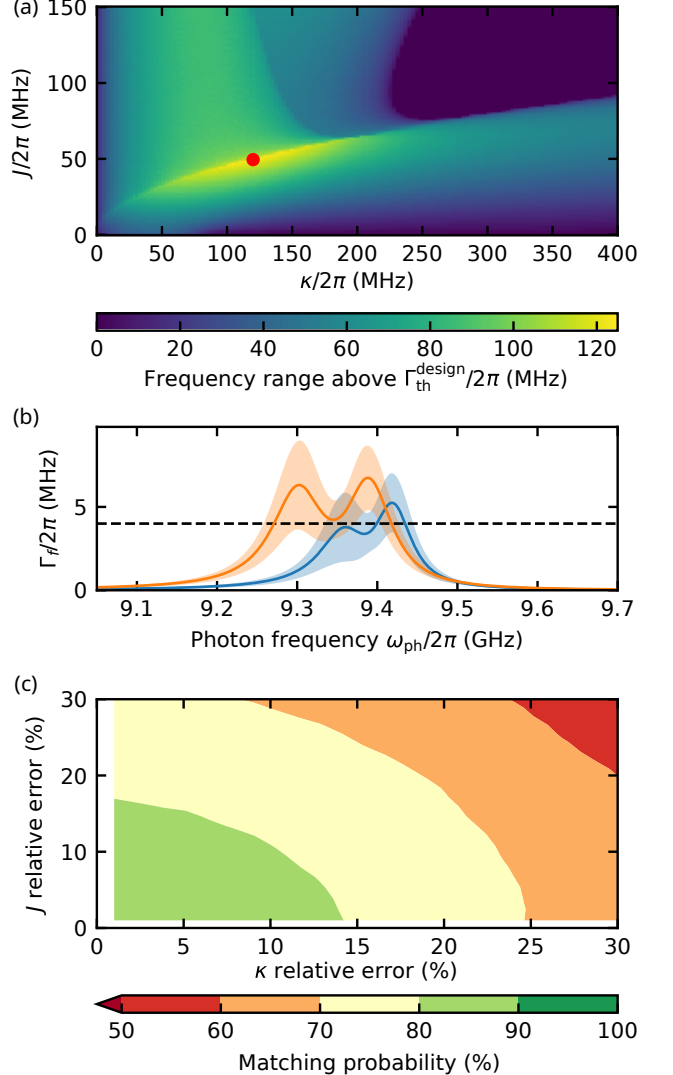


FIG. 6. (a) Frequency range of ω_{ph} that satisfies $\Gamma_f(\omega_{\text{ph}})/2\pi > \Gamma_{\text{th}}^{\text{design}}/2\pi = 8$ MHz. The red circle marks the optimal parameters ($\kappa/2\pi = 120$ MHz, $J/2\pi = 50$ MHz) that maximize the operational bandwidth. (b) Monte Carlo simulation results of Γ_f as a function of photon frequency. The solid lines show the mean photon-emission rate and the shaded regions show the standard deviation for the sender device (blue) and the receiver device (orange). The horizontal dashed line indicates the threshold $\Gamma_{\text{th}}^{\text{MC}}/2\pi = 4$ MHz used in the experiment for evaluating frequency matching. (c) Frequency-matching probability between sender and receiver devices as a function of relative variations in κ and J .

which was chosen as an estimate of the maximum usable drive strength at the design stage.

We sweep the external decay rate κ of the outer resonator and the inter-resonator coupling strength J to find the optimal parameters. This search yields optimal values of $\kappa/2\pi = 120$ MHz and $J/2\pi = 50$ MHz, which maximize the operational bandwidth while maintaining the photon-emission rate above the specified threshold, as shown in Fig. 6(a). These optimized parameters were

used as the basis for the sender device design. The receiver device was designed independently following the Butterworth-filter approach described in the main text.

Note that the actual device parameters slightly differ from these design values due to variations in qubit frequencies and coupling strengths. Consequently, the measured photon-emission rate Γ_f shown in Fig. 6(b) does not reach 8 MHz across the entire frequency range, as the experimental conditions deviate from the idealized design parameters.

3. Monte Carlo simulation of parameter variations

To evaluate the probability of successful frequency matching between independently fabricated sender and receiver devices, we perform Monte Carlo simulations of the transfer-resonator spectrum. We model the complete system using the circuit model corresponding to the fabricated device and calculate the resonator spectrum through electric circuit calculations.

a. Estimation of parameter variations

We assume that the primary source of fabrication uncertainty is the precision limit of photolithography, which we estimate as $\pm 1 \mu\text{m}$ for all geometric features. This tolerance affects both coplanar waveguide lengths and lumped-element capacitor geometries. To translate these geometric variations into circuit parameter uncertainties, we perform finite element electromagnetic simulations incorporating the $1 \mu\text{m}$ tolerance. The capacitance variations obtained from these simulations range from 0.05 to 1.5 fF depending on the capacitor geometry.

To extract the resulting variations in the effective circuit parameters, we calculate the reflection coefficient S_{11} for the complete circuit model including the qubit under different realizations of the geometric tolerances. By fitting these calculated spectra, we obtain estimates of the parameter variations. The resonance frequency of the first resonator shows variations with a standard deviation of approximately 3 MHz, while the second resonator frequency exhibits variations of approximately 20 MHz. The external decay rate and inter-resonator coupling strength both show relative variations of approximately 1%. However, the 3-MHz variation in the first resonator frequency appears smaller than values reported in previous studies. To provide a more conservative estimate consistent with reported frequency variations [40, 41], we adopt a standard deviation of 10 MHz for this parameter in the subsequent Monte Carlo analysis.

b. Monte Carlo simulation

Using the parameter variations chosen above (10 MHz for the inner resonator frequency, 20 MHz for the outer

resonator frequency, 1% relative variation for the external decay rate, and 1% relative variation for the inter-resonator coupling strength), we perform Monte Carlo simulations to evaluate the probability of successful frequency matching between the sender and receiver devices. The nominal parameter values are taken from Table I. We generate 2000 parameter sets by adding Gaussian-distributed random variations to both sender and receiver devices independently.

For each parameter set, we calculate the photon-emission rate $\Gamma_f(\omega_{\text{ph}})$ using Eq. (1). The drive strength for calculating Γ_f is chosen to satisfy the adiabatic conditions $\kappa_+/4 > g_{\text{eff}}$ and $\kappa_-/4 > g_{\text{eff}}$, which ensures that Rabi oscillations are suppressed during the photon emission process. Additionally, the drive strength is kept below $\Omega/2\pi = 750 \text{ MHz}$, beyond which leakage to higher levels can become significant in the experiments. Figure 6(b) shows the mean and standard deviation of $\Gamma_f(\omega_{\text{ph}})$ across the simulated parameter sets for both devices, with the shaded region indicating the mean \pm one standard deviation.

To determine whether a given parameter combination enables successful quantum communication, we check if there exists a common photon frequency ω_{ph} at which both devices satisfy $\Gamma_f(\omega_{\text{ph}})/2\pi \geq \Gamma_{\text{th}}^{\text{MC}}/2\pi = 4 \text{ MHz}$. This threshold corresponds to the photon-emission rate used in the experiments ($\kappa_{\text{ph}}/2\pi = 2 \text{ MHz}$). The lower threshold compared to the value at the design stage ($\Gamma_{\text{th}}^{\text{design}}/2\pi = 8 \text{ MHz}$) reflects several factors. First, the receiver device was designed prioritizing broad bandwidth and flat spectral response without taking into account the photon-emission rate. Second, fabrication-related parameter variations cause the realized devices to deviate from the idealized design parameters. Third, the maximum drive strength used in the experiment ($\Omega/2\pi \sim 750 \text{ MHz}$) was lower than the value used at the design stage ($\Omega/2\pi = 1 \text{ GHz}$).

With these criteria, nearly 90% of the simulated device pairs achieve successful frequency matching within a single fabrication batch.

c. Sensitivity to large parameter variations

The estimated 1% relative variations in the inter-resonator coupling strength J and external decay rate κ may be underestimated due to additional sources of uncertainty not fully captured in our geometric tolerance analysis. To assess the design robustness under more pessimistic scenarios, we perform additional Monte Carlo simulations sweeping the relative variations in J and κ independently from 1% to 30%, while maintaining the frequency variations at 10 MHz and 20 MHz for the first and second resonators, respectively.

Figure 6(c) shows the matching probability as a function of the relative variations in J and κ . The matching probability remains above 50% even when both parameters exhibit 30% relative variations.

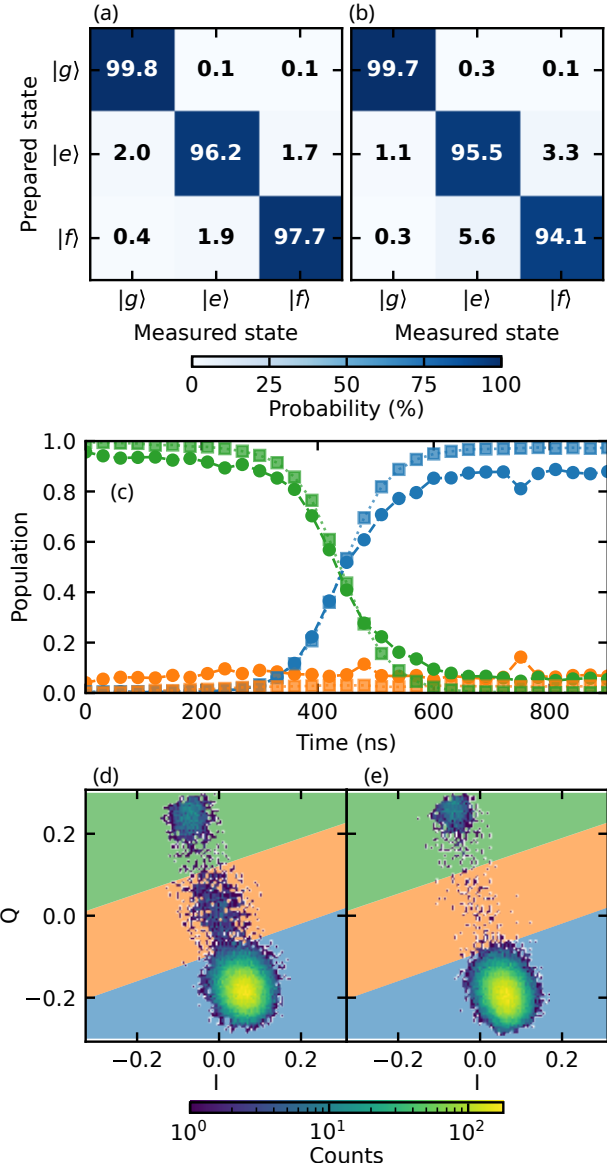


FIG. 7. (a)(b) Readout Assignment matrices for (a) sender and (b) receiver devices. (c) Qubit population after photon emission. Blue, orange, green correspond to the $|g\rangle$, $|e\rangle$, and $|f\rangle$ states. Squares are the sender device and the circles are the receiver device. (d) Single-shot measurement results on the receiver qubit after photon emission. Blue, orange and green areas are assigned to the $|g\rangle$, $|e\rangle$, and $|f\rangle$ states. (e) Single-shot measurement results after photon emission and active reset.

Appendix C: Experimental details

1. Three-state readout

We employ dispersive readout to distinguish the three lowest energy levels of the transmon qubit. To improve the readout fidelity, we use JPA in the degenerate mode.

To establish the classification criteria for three-state readout, we first prepare the qubit in each of the three

states ($|g\rangle$, $|e\rangle$, $|f\rangle$) and perform single-shot measurements to obtain reference distributions on the IQ plane. For each state, we fit a Gaussian Mixture Model (GMM) with two components to the measured distribution and extract the center of the component with the larger weight. We then construct a k -nearest neighbors (k -NN) classifier with $k = 1$ using the three extracted centers as reference points. This classifier partitions the IQ plane into three regions via Voronoi tessellation, each corresponding to one of the qubit states. For each measurement outcome, we classify it into one of the three states based on its position on the IQ plane, and calculate the population of each state as the fraction of outcomes assigned to that state.

From the calibration measurements, we construct the assignment probability matrix R , where R_{ij} represents the probability of assigning outcome j when the qubit is prepared in state i . The assignment matrices for our devices are shown in Fig. 7(a) and (b). To correct for readout errors, similarly to Refs. 24 and 27, we apply matrix inversion to obtain the corrected populations from the measured populations.

2. Qubit population after photon emission

Figure 7(a) shows the qubit population dynamics during the $|f\rangle$ - $|g\rangle$ photon-emission pulse for both devices. We see that the final $|g\rangle$ -state population P_g differs between devices: the sender reaches $P_g = 0.95$ – 0.97 , while the receiver achieves only $P_g = 0.85$ – 0.9 . Since P_g corresponds to the photon-emission efficiency, this imbalance must be accounted for when estimating photon loss.

To investigate the deviation at the receiver, we perform single-shot measurements following photon-emission process. Figure 7(b) reveals that while most population resides in $|g\rangle$, residual population persists in the $|e\rangle$ region and in a region corresponding to the $|f\rangle$ and higher states. Here, our three-state classification assigns all population in the states at or above $|f\rangle$ to a single category, preventing distinction between these levels.

To confirm leakage in $|f\rangle$, we apply active-reset pulses [61] to return the populations in $|e\rangle$ and $|f\rangle$ to $|g\rangle$ before measurement. Figure 7(c) shows that the population remains in the $|f\rangle$ -and-above region after reset, confirming leakage to states above $|f\rangle$. The leakage population exhibits temporal fluctuations, with values ranging from 0.03 to 0.1. The origin of this leakage remains unclear, though possible mechanisms include higher-order transitions or coupling to spurious modes during the emission process [62].

3. State tomography

Quantum state tomography is performed using the single-shot readout method described in Appendix C1. We apply tomography gates prior to measurement and

reconstruct density matrices via maximum-likelihood estimation [24].

For process tomography, qutrit-level measurements on both the sender and receiver are necessary to characterize the population remaining in $|f\rangle$ after state transfer. The process matrix is obtained by projecting the reconstructed qutrit density matrices onto the qubit subspace and applying linear inversion. For Bell-state analysis, we perform two-qutrit tomography and extract the qubit subspace to obtain ρ from the full two-qutrit density matrix $\rho_{3\otimes 3}$ [24, 27].

4. Numerical simulation of quantum communication

Numerical simulations are performed using the cascaded-system formalism [24]. We approximate the two-pole transfer resonators as single-pole resonators for computational simplicity. The effective Hamiltonian and master equation for the cascaded system are

$$\begin{aligned} \mathcal{H}_{\text{eff}} = & -\frac{\alpha_{\text{tx}}}{2} b_{\text{tx}}^\dagger b_{\text{tx}} + \frac{\alpha_{\text{tx}}}{2} b_{\text{tx}}^\dagger b_{\text{tx}}^\dagger b_{\text{tx}} b_{\text{tx}} \\ & -\frac{\alpha_{\text{rx}}}{2} b_{\text{rx}}^\dagger b_{\text{rx}} + \frac{\alpha_{\text{rx}}}{2} b_{\text{rx}}^\dagger b_{\text{rx}}^\dagger b_{\text{rx}} b_{\text{rx}} \\ & + g_{\text{eff}}^{\text{tx}}(t)(a_{\text{tx}} b_{\text{tx}}^\dagger b_{\text{tx}}^\dagger + \text{h.c.})/\sqrt{2} \quad (\text{C1}) \\ & + g_{\text{eff}}^{\text{rx}}(t)(a_{\text{rx}} b_{\text{rx}}^\dagger b_{\text{rx}}^\dagger + \text{h.c.})/\sqrt{2} \\ & -i\frac{\sqrt{\eta\kappa_{\text{tx}}\kappa_{\text{rx}}}}{2}(a_{\text{tx}}^\dagger a_{\text{rx}} - \text{h.c.}) \end{aligned}$$

$$\begin{aligned} \dot{\rho} = & -i[\mathcal{H}_{\text{eff}}, \rho] \\ & + \mathcal{D}[\sqrt{\eta\kappa_{\text{tx}}} a_{\text{tx}} + \sqrt{\kappa_{\text{rx}}} a_{\text{rx}}]\rho + \mathcal{D}[\sqrt{(1-\eta)\kappa_{\text{tx}}} a_{\text{tx}}]\rho \\ & + \sum_{\mu=\text{tx,rx}} \left(\gamma_{1,ge}^\mu \mathcal{D}[|g\rangle\langle e|_\mu] \rho + \gamma_{1,ef}^\mu \mathcal{D}[|e\rangle\langle f|_\mu] \rho \right. \\ & \left. + \gamma_{\phi,ge}^\mu \mathcal{D}[|e\rangle\langle e|_\mu - |g\rangle\langle g|_\mu] \rho + \gamma_{\phi,ef}^\mu \mathcal{D}[|f\rangle\langle f|_\mu - |e\rangle\langle e|_\mu] \rho \right), \quad (\text{C2}) \end{aligned}$$

where $\mathcal{D}[L]\bullet = L \bullet L^\dagger - \{L^\dagger L, \bullet\}/2$ is the dissipation superoperator, $\mu \in \{\text{tx, rx}\}$ labels the device, $\kappa_{\text{tx(rx)}}$ is the transfer-resonator linewidth, η is the photon loss during propagation, $\gamma_{1,ge(ef)}^\mu = 1/T_{1,ge(ef)}^\mu$ is the energy-relaxation rate, and $\gamma_{\phi,ge(ef)}^\mu = 1/T_{2,ge(ef)}^\mu - 1/2T_{1,ge(ef)}^\mu$ is the pure dephasing rate. For the simulations, we use $\kappa_{\text{tx}}/2\pi = 150$ MHz and $\kappa_{\text{rx}}/2\pi = 200$ MHz.

To quantify individual error contributions, we perform simulations under controlled conditions. We isolate photon-loss and absorption-inefficiency contributions by comparing error-free simulations with simulations including only these loss mechanisms (modeled through the loss parameter η). The absorption inefficiency arises from waveform mismatch between emission and absorption processes; in our simulations, we assume perfect waveform matching and incorporate the measured absorption inefficiency directly into η . Under

these assumptions, the specific values of κ_{tx} and κ_{rx} have negligible impact on the simulation results. De-coherence contributions from T_1 and T_ϕ are estimated by comparing simulations with photon loss (but with infinite coherence times) against simulations with finite T_1 and/or T_ϕ .

[1] Google Quantum AI and Collaborators, Quantum error correction below the surface code threshold, *Nature* **638**, 920 (2025).

[2] N. Lacroix, A. Bourassa, F. J. H. Heras, *et al.*, Scaling and logic in the colour code on a superconducting quantum processor, *Nature* **645**, 614 (2025).

[3] M. Webber, V. Elfving, S. Weidt, and W. K. Hensinger, The impact of hardware specifications on reaching quantum advantage in the fault tolerant regime, *AVS Quantum Science* **4**, 013801 (2022).

[4] S. Bravyi, O. Dial, J. M. Gambetta, D. Gil, and Z. Nazario, The future of quantum computing with superconducting qubits, *Journal of Applied Physics* **132**, 160902 (2022).

[5] M. Mohseni, A. Scherer, K. G. Johnson, O. Wertheim, M. Otten, N. A. Aadit, Y. Alexeev, K. M. Bresniker, K. Y. Camsari, B. Chapman, S. Chatterjee, G. A. Dagnow, A. Esposito, F. Fahim, M. Fiorentino, A. Gajjar, A. Khalid, X. Kong, B. Kulchytskyy, E. Kyoseva, R. Li, P. A. Lott, I. L. Markov, R. F. McDermott, G. Pedretti, P. Rao, E. Rieffel, A. Silva, J. Sorebo, P. Spentzouris, Z. Steiner, B. Torosov, D. Venturelli, R. J. Visser, Z. Webb, X. Zhan, Y. Cohen, P. Ronagh, A. Ho, R. G. Beausoleil, and J. M. Martinis, How to Build a Quantum Supercomputer: Scaling from Hundreds to Millions of Qubits (2025), arXiv:2411.10406.

[6] N. Raicu, T. Hogan, X. Wu, M. Vahidpour, D. Snow, M. Hollister, and M. Field, Cryogenic thermal modeling of microwave high density signaling, *EPJ Quantum Technol.* **12**, 124 (2025).

[7] S. Krinner, S. Storz, P. Kurpiers, P. Magnard, J. Heinssoo, R. Keller, J. Lütfolf, C. Eichler, and A. Wallraff, Engineering cryogenic setups for 100-qubit scale superconducting circuit systems, *EPJ Quantum Technol.* **6**, 2 (2019).

[8] J. B. Hertzberg, E. J. Zhang, S. Rosenblatt, E. Magesan, J. A. Smolin, J.-B. Yau, V. P. Adiga, M. Sandberg, M. Brink, J. M. Chow, and J. S. Orcutt, Laser-annealing Josephson junctions for yielding scaled-up superconducting quantum processors, *npj Quantum Inf.* **7**, 129 (2021).

[9] J. Ang, G. Carini, Y. Chen, I. Chuang, M. Demarco, S. Economou, A. Eickbusch, A. Faraon, K.-M. Fu, S. Girvin, M. Hatridge, A. Houck, P. Hilaire, K. Krsulich, A. Li, C. Liu, Y. Liu, M. Martonosi, D. McKay, J. Misiewich, M. Ritter, R. Schoelkopf, S. Stein, S. Sussman, H. Tang, W. Tang, T. Tomesh, N. Tubman, C. Wang, N. Wiebe, Y. Yao, D. Yost, and Y. Zhou, ARQUIN: Architectures for Multinode Superconducting Quantum Computers, *ACM Transactions on Quantum Computing* **5**, 1 (2024).

[10] M. Caleffi, M. Moretti, D. Ferrari, J. Illiano, A. Manzalini, and A. S. Cacciapuoti, Distributed quantum computing: A survey, *Computer Networks* **254**, 110672 (2024).

[11] J. I. Cirac, P. Zoller, H. J. Kimble, and H. Mabuchi, Quantum State Transfer and Entanglement Distribution among Distant Nodes in a Quantum Network, *Phys. Rev. Lett.* **78**, 3221 (1997).

[12] Y. P. Zhong, H.-S. Chang, K. J. Satzinger, M.-H. Chou, A. Bienfait, C. R. Conner, E. Dumur, J. Grebel, G. A. Peairs, R. G. Povey, D. I. Schuster, and A. N. Cleland, Violating Bell's inequality with remotely connected superconducting qubits, *Nat. Phys.* **15**, 741 (2019).

[13] N. Leung, Y. Lu, S. Chakram, R. K. Naik, N. Earnest, R. Ma, K. Jacobs, A. N. Cleland, and D. I. Schuster, Deterministic bidirectional communication and remote entanglement generation between superconducting qubits, *npj Quantum Inf.* **5**, 18 (2019).

[14] H.-S. Chang, Y. Zhong, A. Bienfait, M.-H. Chou, C. Conner, E. Dumur, J. Grebel, G. Peairs, R. Povey, K. Satzinger, and A. Cleland, Remote Entanglement via Adiabatic Passage Using a Tunably Dissipative Quantum Communication System, *Phys. Rev. Lett.* **124**, 240502 (2020).

[15] L. D. Burkhardt, J. D. Teoh, Y. Zhang, C. J. Axline, L. Frunzio, M. Devoret, L. Jiang, S. Girvin, and R. Schoelkopf, Error-Detected State Transfer and Entanglement in a Superconducting Quantum Network, *PRX Quantum* **2**, 030321 (2021).

[16] Y. Zhong, H.-S. Chang, A. Bienfait, E. Dumur, M.-H. Chou, C. R. Conner, J. Grebel, R. G. Povey, H. Yan, D. I. Schuster, and A. N. Cleland, Deterministic multi-qubit entanglement in a quantum network, *Nature* **590**, 571 (2021).

[17] J. Niu, L. Zhang, Y. Liu, J. Qiu, W. Huang, J. Huang, H. Jia, J. Liu, Z. Tao, W. Wei, Y. Zhou, W. Zou, Y. Chen, X. Deng, X. Deng, C. Hu, L. Hu, J. Li, D. Tan, Y. Xu, F. Yan, T. Yan, S. Liu, Y. Zhong, A. N. Cleland, and D. Yu, Low-loss interconnects for modular superconducting quantum processors, *Nat Electron* **6**, 10.1038/s41928-023-00925-z (2023).

[18] J. Qiu, Z. Zhang, Z. Wang, L. Zhang, Y. Zhou, X. Sun, J. Zhang, X. Linpeng, S. Liu, J. Niu, Y. Zhong, and D. Yu, A thermal-noise-resilient microwave quantum network traversing 4 K (2025), arXiv:2503.01133.

[19] K. Heya, T. Phung, M. Malekakhlagh, R. Steiner, M. Turchetti, W. Shanks, J. Mamin, W.-S. Lu, Y. P. Kandel, N. Sundaresan, and J. Orcutt, Randomized Benchmarking of a Remote cnot Gate Via a Meter-Scale Microwave Link, *Phys. Rev. Lett.* **135**, 200801 (2025).

[20] J. Song, S. Yang, P. Liu, H.-L. Zhang, G.-M. Xue, Z.-Y. Mi, W.-G. Zhang, F. Yan, Y.-R. Jin, and H.-F. Yu, Realization of High-Fidelity Perfect Entanglers between Remote Superconducting Quantum Processors, *Phys. Rev. Lett.* **135**, 050603 (2025).

[21] M. Mollenhauer, A. Irfan, X. Cao, S. Mandal, and W. Pfaff, A high-efficiency elementary network of interchangeable superconducting qubit devices, *Nat Electron* **8**, 610 (2025).

[22] Y. Li, X. Zhang, W. Zhang, R. Guo, Y. Zhang, X. Tan, and Y. Yu, Fast and Robust Remote Two-Qubit Gates on Distributed Qubits (2025), arXiv:2511.01418.

[23] M. Casariego, E. Zambrini Cruzeiro, S. Gherardini, T. Gonzalez-Raya, R. André, G. Frazão, G. Catto, M. Möttönen, D. Datta, K. Viisanen, J. Govenius, M. Prunnila, K. Tuominen, M. Reichert, M. Renger, K. G. Fedorov, F. Deppe, H. Van Der Vliet, A. J. Matthews, Y. Fernández, R. Assouly, R. Dassonneville, B. Huard, M. Sanz, and Y. Omar, Propagating quantum microwaves: towards applications in communication and sensing, *Quantum Sci. Technol.* **8**, 023001 (2023).

[24] P. Kurpiers, P. Magnard, T. Walter, B. Royer, M. Pechal,

J. Heinsoo, Y. Salathé, A. Akin, S. Storz, J.-C. Besse, S. Gasparinetti, A. Blais, and A. Wallraff, Deterministic quantum state transfer and remote entanglement using microwave photons, *Nature* **558**, 264 (2018).

[25] P. Campagne-Ibarcq, E. Zalys-Geller, A. Narla, S. Shankar, P. Reinhold, L. Burkhardt, C. Axline, W. Pfaff, L. Frunzio, R. Schoelkopf, and M. Devoret, Deterministic Remote Entanglement of Superconducting Circuits through Microwave Two-Photon Transitions, *Phys. Rev. Lett.* **120**, 200501 (2018).

[26] C. J. Axline, L. D. Burkhardt, W. Pfaff, M. Zhang, K. Chou, P. Campagne-Ibarcq, P. Reinhold, L. Frunzio, S. M. Girvin, L. Jiang, M. H. Devoret, and R. J. Schoelkopf, On-demand quantum state transfer and entanglement between remote microwave cavity memories, *Nature Phys* **14**, 705 (2018).

[27] P. Magnard, S. Storz, P. Kurpiers, J. Schär, F. Marxer, J. Lütolf, T. Walter, J.-C. Besse, M. Gabureac, K. Reuer, A. Akin, B. Royer, A. Blais, and A. Wallraff, Microwave Quantum Link between Superconducting Circuits Housed in Spatially Separated Cryogenic Systems, *Phys. Rev. Lett.* **125**, 260502 (2020).

[28] S. Storz, J. Schär, A. Kulikov, P. Magnard, P. Kurpiers, J. Lütolf, T. Walter, A. Copetudo, K. Reuer, A. Akin, J.-C. Besse, M. Gabureac, G. J. Norris, A. Rosario, F. Martin, J. Martinez, W. Amaya, M. W. Mitchell, C. Abellán, J.-D. Bancal, N. Sangouard, B. Royer, A. Blais, and A. Wallraff, Loophole-free Bell inequality violation with superconducting circuits, *Nature* **617**, 265 (2023).

[29] A. Kulikov, S. Storz, J. D. Schär, M. Sandfuchs, R. Wolf, F. Berterotti, C. Hellings, R. Renner, and A. Wallraff, Device-Independent Randomness Amplification (2024), arXiv:2412.17931.

[30] S. Storz, A. Kulikov, J. D. Schär, V. Barizien, X. Valcarce, F. Berterotti, N. Sangouard, J.-D. Bancal, and A. Wallraff, Complete Self-Testing of a System of Remote Superconducting Qubits, *Phys. Rev. Lett.* **135**, 030801 (2025).

[31] A. Narla, S. Shankar, M. Hatridge, Z. Leghtas, K. Sliwa, E. Zalys-Geller, S. Mundhada, W. Pfaff, L. Frunzio, R. Schoelkopf, and M. Devoret, Robust Concurrent Remote Entanglement Between Two Superconducting Qubits, *Phys. Rev. X* **6**, 031036 (2016).

[32] J. Qiu, Y. Liu, L. Hu, Y. Wu, J. Niu, L. Zhang, W. Huang, Y. Chen, J. Li, S. Liu, Y. Zhong, L. Duan, and D. Yu, Deterministic quantum state and gate teleportation between distant superconducting chips, *Science Bulletin* **70**, 351 (2025).

[33] J. Grebel, H. Yan, M.-H. Chou, G. Andersson, C. R. Conner, Y. J. Joshi, J. M. Miller, R. G. Povey, H. Qiao, X. Wu, and A. N. Cleland, Bidirectional Multiphoton Communication between Remote Superconducting Nodes, *Phys. Rev. Lett.* **132**, 047001 (2024).

[34] A. Almanakly, B. Yankelevich, M. Hays, B. Kannan, R. Assouly, A. Greene, M. Gingras, B. M. Niedzielski, H. Stickler, M. E. Schwartz, K. Serniak, J. I.-j. Wang, T. P. Orlando, S. Gustavsson, J. A. Grover, and W. D. Oliver, Deterministic remote entanglement using a chiral quantum interconnect, *Nat. Phys.* **21**, 825 (2025).

[35] P. Krantz, M. Kjaergaard, F. Yan, T. P. Orlando, S. Gustavsson, and W. D. Oliver, A quantum engineer's guide to superconducting qubits, *Applied Physics Reviews* **6**, 021318 (2019).

[36] T. Miyamura, Y. Sunada, Z. Wang, J. Ilves, K. Mat-suura, and Y. Nakamura, Generation of Frequency-Tunable Shaped Single Microwave Photons Using a Fixed-Frequency Superconducting Qubit, *PRX Quantum* **6**, 020347 (2025).

[37] J. Koch, T. M. Yu, J. Gambetta, A. A. Houck, D. I. Schuster, J. Majer, A. Blais, M. H. Devoret, S. M. Girvin, and R. J. Schoelkopf, Charge-insensitive qubit design derived from the Cooper pair box, *Phys. Rev. A* **76**, 042319 (2007).

[38] M. Pechal, L. Huthmacher, C. Eichler, S. Zeytinoğlu, A. Abdumalikov, S. Berger, A. Wallraff, and S. Philipp, Microwave-Controlled Generation of Shaped Single Photons in Circuit Quantum Electrodynamics, *Phys. Rev. X* **4**, 041010 (2014).

[39] S. Zeytinoğlu, M. Pechal, S. Berger, A. A. Abdumalikov, A. Wallraff, and S. Philipp, Microwave-induced amplitude- and phase-tunable qubit-resonator coupling in circuit quantum electrodynamics, *Phys. Rev. A* **91**, 043846 (2015).

[40] Y. Li, T. Wang, J. Hu, D. Li, and S. An, Optimizing Resonator Frequency Stability in Flip-Chip Architectures: A Novel Experimental Design Approach (2023), arXiv:2312.06405.

[41] S. Vallés-Sanclemente, S. L. M. Van Der Meer, M. Finkel, N. Muthusubramanian, M. Beekman, H. Ali, J. F. Marques, C. Zachariadis, H. M. Veen, T. Stavenga, N. Haider, and L. DiCarlo, Post-fabrication frequency trimming of coplanar-waveguide resonators in circuit QED quantum processors, *Applied Physics Letters* **123**, 034004 (2023).

[42] T. Thorbeck, A. McDonald, O. Lanes, J. Blair, G. Keefe, A. A. Stabile, B. Royer, L. C. G. Goria, and A. Blais, High-fidelity gates in a transmon using bath engineering for passive leakage reset (2024), arXiv:2411.04101.

[43] E. A. Sete, J. M. Martinis, and A. N. Korotkov, Quantum theory of a bandpass Purcell filter for qubit readout, *Phys. Rev. A* **92**, 012325 (2015).

[44] E. Jeffrey, D. Sank, J. Mutus, T. White, J. Kelly, R. Barends, Y. Chen, Z. Chen, B. Chiaro, A. Dunsworth, A. Megrant, P. O'Malley, C. Neill, P. Roushan, A. Vainsencher, J. Wenner, A. Cleland, and J. M. Martinis, Fast Accurate State Measurement with Superconducting Qubits, *Phys. Rev. Lett.* **112**, 190504 (2014).

[45] Y. Sunada, S. Kono, J. Ilves, S. Tamate, T. Sugiyama, Y. Tabuchi, and Y. Nakamura, Fast Readout and Reset of a Superconducting Qubit Coupled to a Resonator with an Intrinsic Purcell Filter, *Phys. Rev. Applied* **17**, 044016 (2022).

[46] Y. Sunada, K. Yuki, Z. Wang, T. Miyamura, J. Ilves, K. Matsuura, P. A. Spring, S. Tamate, S. Kono, and Y. Nakamura, Photon-Noise-Tolerant Dispersive Readout of a Superconducting Qubit Using a Nonlinear Purcell Filter, *PRX Quantum* **5**, 010307 (2024).

[47] P. A. Spring, L. Milanovic, Y. Sunada, S. Wang, A. F. van Loo, S. Tamate, and Y. Nakamura, Fast Multiplexed Superconducting-Qubit Readout with Intrinsic Purcell Filtering Using a Multiconductor Transmission Line, *PRX Quantum* **6**, 020345 (2025).

[48] T. Yamamoto, K. Inomata, M. Watanabe, K. Matsuba, T. Miyazaki, W. D. Oliver, Y. Nakamura, and J. S. Tsai, Flux-driven Josephson parametric amplifier, *Appl. Phys. Lett.* **93**, 042510 (2008).

[49] I. L. Chuang and M. A. Nielsen, Prescription for experimental determination of the dynamics of a quantum black box, *Journal of Modern Optics* **44**, 2455 (1997).

[50] C. Müller, J. Lisenfeld, A. Shnirman, and S. Poletto, Interacting two-level defects as sources of fluctuating high-frequency noise in superconducting circuits, *Phys. Rev. B* **92**, 035442 (2015).

[51] P. Klimov, J. Kelly, Z. Chen, M. Neeley, A. Megrant, B. Burkett, R. Barends, K. Arya, B. Chiaro, Y. Chen, A. Dunsworth, A. Fowler, B. Foxen, C. Gidney, M. Giustina, R. Graff, T. Huang, E. Jeffrey, E. Lucero, J. Mutus, O. Naaman, C. Neill, C. Quintana, P. Roushan, D. Sank, A. Vainsencher, J. Wenner, T. White, S. Boixo, R. Babbush, V. Smelyanskiy, H. Neven, and J. Martinis, Fluctuations of Energy-Relaxation Times in Superconducting Qubits, *Phys. Rev. Lett.* **121**, 090502 (2018).

[52] T. Thorbeck, A. Eddins, I. Lauer, D. T. McClure, and M. Carroll, Two-Level-System Dynamics in a Superconducting Qubit Due to Background Ionizing Radiation, *PRX Quantum* **4**, 020356 (2023).

[53] O. Gargiulo, S. Oleschko, J. Prat-Camps, M. Zanner, and G. Kirchmair, Fast flux control of 3D transmon qubits using a magnetic hose, *Applied Physics Letters* **118**, 012601 (2021).

[54] A. Krasnok, P. Dhakal, A. Fedorov, P. Frigola, M. Kelly, and S. Kutsaev, Superconducting microwave cavities and qubits for quantum information systems, *Applied Physics Reviews* **11**, 011302 (2024).

[55] G. F. Peñas, R. Puebla, and J. J. García-Ripoll, Multiplexed quantum state transfer in waveguides, *Phys. Rev. Research* **6**, 033294 (2024).

[56] J. Yang, M. Khanahmadi, I. Strandberg, A. Gaikwad, C. Castillo-Moreno, A. F. Kockum, M. A. Ullah, G. Johansson, A. M. Eriksson, and S. Gasparinetti, Deterministic Generation of Frequency-Bin-Encoded Microwave Photons, *Phys. Rev. Lett.* **134**, 240803 (2025).

[57] J. O’Sullivan, K. Reuer, A. Grigorev, X. Dai, A. Hernández-Antón, M. H. Muñoz-Arias, C. Hellings, A. Flasby, D. Colao Zanuz, J.-C. Besse, A. Blais, D. Malz, C. Eichler, and A. Wallraff, Deterministic generation of two-dimensional multi-photon cluster states, *Nat Commun* **16**, 5505 (2025).

[58] Z. Wang, T. Miyamura, Y. Sunada, K. Sunada, J. Ilves, K. Matsuura, and Y. Nakamura, Generation of frequency-bin-encoded dual-rail cluster states via time-frequency multiplexing of microwave photonic qubits (2025), arXiv:2508.10990.

[59] C. Müller, J. H. Cole, and J. Lisenfeld, Towards understanding two-level-systems in amorphous solids: insights from quantum circuits, *Rep. Prog. Phys.* **82**, 124501 (2019).

[60] J. Ilves, S. Kono, Y. Sunada, S. Yamazaki, M. Kim, K. Koshino, and Y. Nakamura, On-demand generation and characterization of a microwave time-bin qubit, *npj Quantum Inf.* **6**, 34 (2020).

[61] P. Magnard, P. Kurpiers, B. Royer, T. Walter, J.-C. Besse, S. Gasparinetti, M. Pechal, J. Heinsoo, S. Storz, A. Blais, and A. Wallraff, Fast and Unconditional All-Microwave Reset of a Superconducting Qubit, *Phys. Rev. Lett.* **121**, 060502 (2018).

[62] W. Dai, S. Hazra, D. K. Weiss, P. D. Kurilovich, T. Connolly, H. K. Babla, S. Singh, V. R. Joshi, A. Z. Ding, P. D. Parakh, J. Venkatraman, X. Xiao, L. Frunzio, and M. H. Devoret, Spectroscopy of drive-induced unwanted state transitions in superconducting circuits (2025), arXiv:2506.24070.